

Neutronic analysis of the fusion reactor ARC: Monte Carlo
simulations with the Serpent code

Alex Aimetta,^{*,a} Nicolò Abrate,^a Sandra Dulla,^a and Antonio Froio^a

*^aPolitecnico di Torino, Dipartimento Energia, NEMO group
Corso Duca degli Abruzzi, 24 - 10129 Torino (Italy)*

*Email: alex.aimetta@polito.it

Number of pages: 29
Number of tables: 8
Number of figures: 14

Neutronic analysis of the fusion reactor ARC: Monte Carlo simulations with the Serpent code

Alex Aimetta, Nicolò Abrate, Sandra Dulla, and Antonio Froio

Abstract

The neutronic modelling of fusion machines requires the detailed representation of their complex geometry in order to properly evaluate various parameters of interests, such as the energy deposition and the tritium production in the breeding blanket. In this work, the neutronics of the Affordable, Robust and Compact (ARC) fusion reactor is modeled with the Monte Carlo particle transport code Serpent, developed at VTT Technical Research Centre of Finland, as an alternative to the other, more established tools in the fusion community, such as the MCNP (Monte Carlo N-Particle Transport) code. The evaluation of the tritium breeding ratio and the power deposited by neutrons and photons inside the breeding blanket of ARC is performed. Considerations related to the activation of materials and to the neutron shielding are not taken into account. As a first step, the estimations have been obtained adopting a spatially uniform neutron source inside the plasma chamber. A second set of calculations has been performed considering a non-uniform source which takes into account a more realistic neutron generation distribution, with higher values at the centre of the plasma and reduced rates towards the plasma edge. The results obtained with Serpent have been compared with available literature values for the TBR and the power deposition, confirming that Serpent can be considered a suitable alternative code for the neutronic analysis of fusion reactors like ARC. The TBR presented in this article (1.0853) is in good agreement with the value found in the literature, with a relative difference of 0.49%. The total power deposition has a maximum relative difference of 12% for the components of interest in the present work.

Keywords Neutronics, Affordable Robust Compact (ARC), Fusion, Monte Carlo, Serpent

I. INTRODUCTION

The Affordable Robust Compact (ARC) reactor¹ (fig. 1) is a small D-T based tokamak design aimed at the production of electric power, with a significant size reduction with respect to other next-generation machines, such as DEMO (DEMONstration Power Plant). In fact, the fusion power of ARC is estimated around 525 MW, with an electrical output of 200 MWe, compared to the foreseen 1000 MWe for the EU-DEMO.² The main driver of the ARC design is to reduce the reactor size and, as a consequence, its cost and complexity, with respect to traditional fusion machine designs, whilst maintaining a considerable power output. This will be achieved by increasing the magnetic field intensity, employing high-temperature superconductors in place of the traditional, low-temperature ones, as will be adopted in ITER, the world's largest magnetic confinement tokamak currently being constructed in the south of France.

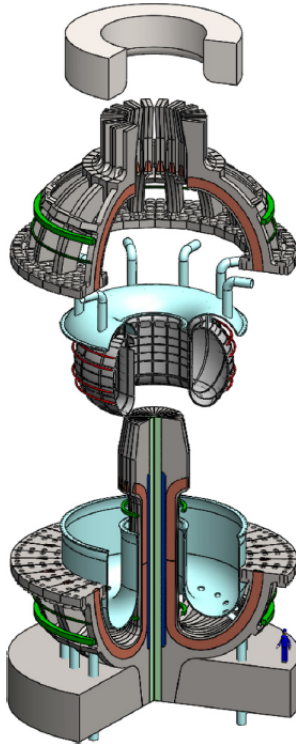


Fig. 1. ARC assembling scheme (reproduced from¹).

The current design of ARC foresees a breeding blanket of the "liquid immersion" type, i.e. the vacuum vessel is submerged in a pool filled with a molten salt, i.e. FLiBe. The FLiBe salt

works simultaneously as neutron multiplier, neutron moderator, shield, heat transfer fluid, breeder, and tritium carrier, and it is continuously circulated. To breed a sufficient amount of tritium, the lithium in the salt is isotopically enriched in ${}^6\text{Li}$ up to 90%, whereas the neutron economy is enhanced by the presence of beryllium, acting as a neutron multiplier.

The neutrons produced inside the plasma chamber reach the FLiBe blanket after crossing the vacuum vessel; in the blanket, neutrons breed tritium through interactions with lithium and deposit their energy within the circulating molten salt, which is then sent to a heat exchanger for power conversion.

The present work is focused on the neutronic analysis of ARC, performed with the Monte Carlo particle transport code Serpent 2 (v. 2.1.31),³ developed at VTT Technical Research Centre of Finland, since 2004. Despite this code has been mainly developed and validated for fission reactor analyses, recent benchmarking activities with the MCNP code⁴ have been carried out successfully also for fusion machines.^{5,6,7}

The neutronic analysis focuses on two specific quantities, chosen for their prominent importance in the context of fusion technology development: the Tritium Breeding Ratio (TBR) and the power deposited by neutrons inside the breeding blanket. The first is the parameter employed to assess whether the fuel cycle of a fusion machine design can be closed ($\text{TBR}>1$) or not ($\text{TBR}<1$), taking into account losses, inefficiencies, and the tritium inventory needed to start up another plant; the latter is directly linked to the net electrical power produced by the plant. Both parameters are evaluated considering two different plasma source models of increasing physical detail.

The simulation of neutron propagation in the complex geometries characterizing a fusion machine typically requires the use of Monte Carlo codes, allowing to properly describe the energetic aspects thanks to continuous-energy cross-sections for neutron-induced interactions. It must be noted though that the nuclear data related to some materials adopted in fusion reactors can be affected by considerable uncertainty, both because there are chemical elements not typically adopted in fission reactors (e.g. fluorine and lithium in FLiBe), and because of the higher energy range of fusion neutrons. Therefore, it is of paramount importance to make use of reliable codes for the simulation of neutron transport and of high-quality nuclear data libraries.

II. MODELLING OF ARC BREEDING BLANKET

II.A. Serpent geometry model of the breeding blanket

The modelling of ARC blanket in this work is carried out with the Serpent code exploiting the acquired expertise in the use of this code in the frame of fission reactor research,^{8,9} taking also profit of the fact that it has been proven in a recent application to allow to handle complex geometries (typical of fusion reactors) in a simpler and faster manner with respect to MCNP.⁵ In fact, Serpent is not only based on the Constructed Solid Geometry (CSG) approach, but it offers the opportunity to directly import CAD-based geometry types exploiting the stereolithography (STL) format too. This feature is particularly useful in the case of complex geometries, typical of fusion reactor designs as ARC.

Hence, in this work, the geometry of the ARC reactor has been developed using the SolidWorks CAD software,¹⁰ exploiting the few information retrieved from the literature¹¹ on the geometrical dimensions of the machine, subsequently imported in Serpent using the STL format. Since ARC's design is still in its conceptual stage, precise information about the dimension of some components is not yet available. This fact furtherly justifies the use of SolidWorks, as it offers the opportunity to continuously update the CAD geometrical model according to the new design input. For instance, recent studies suggest that a change of the thicknesses of the layers composing the vacuum vessel might further improve the performance of ARC.¹² Table I shows the thicknesses as adopted in our study and the corresponding material.

TABLE I
Radial thickness of the double vacuum vessel layers.¹¹

	Thickness [cm]	Material
First wall	0.1	Tungsten
Inner VV	1	Inconel 718
Cooling channel	2	FLiBe
Neutron multiplier	1	Beryllium
Outer VV	3	Inconel 718

The volumes obtained with the CAD model developed are in good agreement with the values found in the literature, as shown in Table II.

The only component affected by a non-negligible difference in volume is the FLiBe breeding blanket, but it is reasonable to believe that this difference does not affect considerably the final

TABLE II
Volumes of each material layer in the ARC reactor.

	Volumes (CAD model) [m ³]	Volumes ¹¹ [m ³]	Relative difference [%]
Plasma	147	137	7.3
First wall	0.32	0.35	8.6
Inner VV	3.27	3.50	6.6
Cooling channel	6.58	7.04	6.5
Neutron multiplier	3.31	3.55	6.8
Outer VV	10.0	10.7	6.5
FLiBe blanket	304	241	26.1
PF coil shielding	43.5	49.2	11.6

results, since previous studies have proved that the neutron flux is reduced by two orders of magnitude when moving around 70 cm inside the blanket.¹² This means that, even if the volume of the blanket in our model is slightly larger, the amount of tritium produced and the power deposited in the peripheral regions can be considered as negligible and will not have remarkable consequences on the final results. However, future studies will iterate the blanket size to optimise nuclear responses.

Other components, such as the poloidal field coils, the toroidal field coils and the central solenoid are not considered in Table II, as they are not relevant in the context of this work, focused on the TBR and the power deposition inside the blanket tank.

Other dimensions adopted in order to define the ARC geometry with the CAD model, which can be useful to reproduce the present model, are listed in table III.

TABLE III
Main dimensions of the ARC reactor adopted in the CAD model.

	Length [cm]
Major radius	330
Minor radius	110
Radius of the outer blanket tank surface	563
Height of the outer blanket tank surface	716
Height of the VV up to the divertor leg	405
Vertical distance between the centres of the divertors	617
Thickness of the inboard breeding blanket	70
Thickness of the ZrH ₂ neutron shielding	25

Figure 2(a) shows a CAD drawing of the blanket of ARC, including with the plasma chamber

and the vacuum vessel, generated with SolidWorks and imported into the Serpent simulations using the STL format. In fig. 2(b) the layered composition of the vacuum vessel is shown. The consistency of the imported geometry has been checked with the `-checkstl` option available in Serpent.

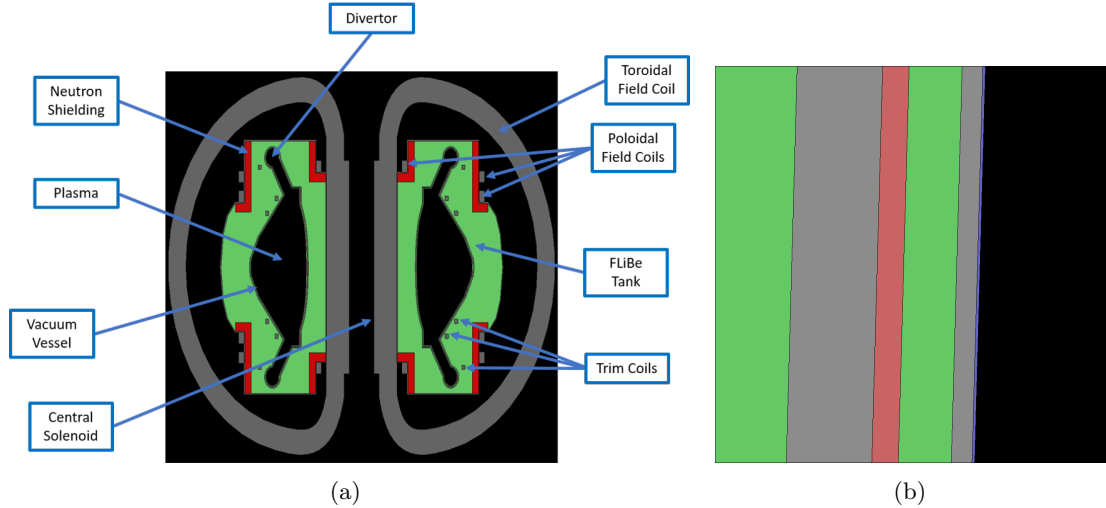


Fig. 2. Poloidal section of ARC generated with the CAD model and implemented in Serpent (a), and detail of the radial build of the double wall vacuum vessel (b). From the right to the left: plasma chamber (black), first wall (blue), inner vacuum vessel (grey), cooling channel (green), neutron multiplier (red), outer vacuum vessel (grey) and FLiBe blanket (green).

Another fundamental parameter that influences the neutron flux and all the related quantities (i.e, TBR and neutron power deposition) is the temperature field in the different components, as it influences the macroscopic cross section of neutron interactions. A positive aspect of using the Serpent 2 code is its capability of performing an automatic adjustments of the nuclear data according to the temperature defined in each material composition. Therefore, in order to properly define the neutronic model, it is also necessary to know the temperature field in each ARC component. The present work, to the authors' knowledge, is the first attempt to model ARC with Serpent, so it has been assumed that each material is featured by an average temperature, deduced by a temperature profile obtained using COMSOL (fig. 3) and presented in a previous work.¹ In this respect, a future development of the model will require the coupling to a thermal-hydraulic model, to obtain a more realistic temperature field and reduce the extent of the uniform approximation here adopted. In future works, the reliability of Serpent might be checked in this context too, since the code allows to exploit a multi-physics coupling scheme thanks to the so-called *universal multi-physics interface*, which has been recently exploited with the OpenFOAM toolkit.¹³

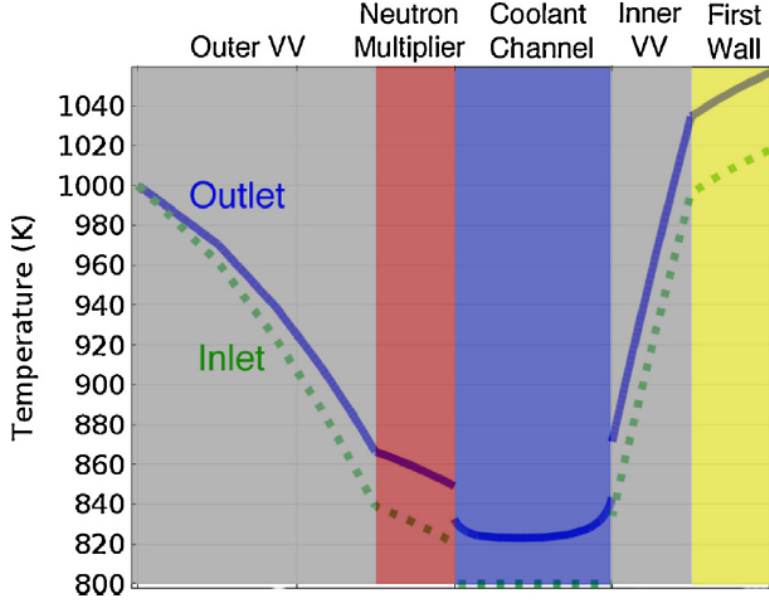


Fig. 3. Temperature distribution across the vacuum vessel (with the plasma-facing surface on right) at both the channel inlet and outlet, evaluated with a COMSOL model (reproduced from¹).

II.B. Neutron source definition

In spite of the fact that Serpent has mainly been developed for fission applications, it is also adequate to analyse systems injected by an external neutron source, e.g. fusion devices. However, Serpent is still defective for what concerns the definition of the source features, which in our case are extremely complex and strictly related to plasma physics phenomena. For this reason, the addition of a plasma source subroutine similar to the one present in MCNP should be considered,¹⁴ while in this work different, imposed distributions of the neutron source have been tested.

At first, a spatially uniform source has been defined, covering the whole plasma chamber except for the two divertor legs, where few neutrons are expected to be produced. The source has been set as monoenergetic, since all the neutrons are generated with an energy of 14.1 MeV. The Serpent code has not been developed to model complex and anisotropic sources. Therefore, an isotropic neutron emission has been defined, which is consistent with the fact that the neutron propagation in the plasma is not influenced by the magnetic field.

The source rate normalization is estimated as follows: considering that around 80% of the ARC fusion power, equal to 525 MW, is carried by neutrons, and that all the neutrons emitted by the source are at 14.1 MeV, a source rate equal to 1.86×10^{20} neutrons/s is obtained.

As a next step, an attempt to obtain a more realistic source spatial distribution has been carried out, still maintaining the monoenergetic and isotropic features. In order to simulate the fact that the neutron emission is higher in the centre of the plasma, where the temperature reaches its maximum, and declines approaching the plasma edge, different weights are assigned to different locations inside the plasma chamber. According to a previous work,¹ the temperature and density distributions in ARC, expressed as a function of the ratio between the radial coordinate r and the minor radius a , are the ones shown in fig. 4. From the electron density graph it is possible

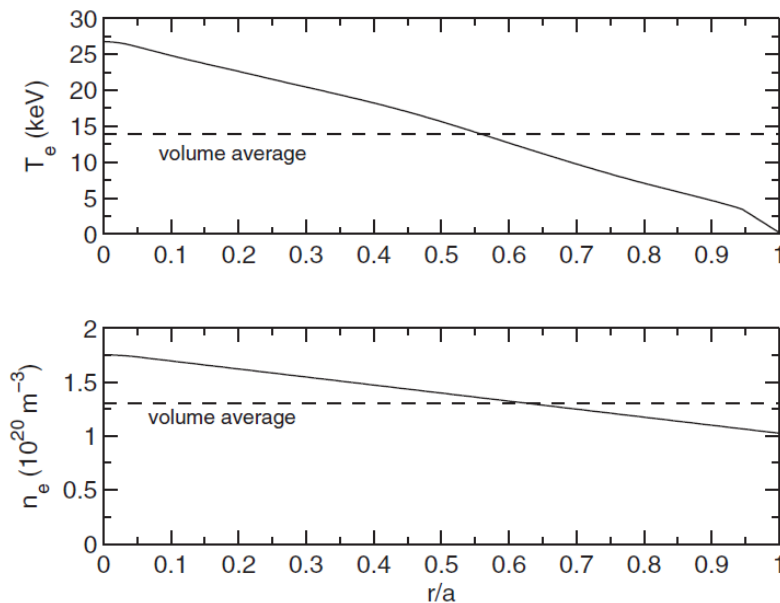


Fig. 4. Radial profiles of electron temperature and electron density in ARC (reproduced from¹)

to extract the density of deuterium and tritium, since, due to the quasi-neutrality condition, the total positive charge is equal to the negative one and the deuterium and tritium densities can be assumed equal in order to maximize the fusion power. As a consequence, the densities of the two hydrogen isotopes inside the plasma chamber can be obtained simply dividing by a factor two the electron density.

Knowing the temperature distribution, it is straightforward to get the D-T reactivity ($\overline{\sigma v}$) as a function of the temperature, expressed in keV, thanks to the following correlation:¹⁵

$$(\overline{\sigma v})_{DT} = 3.68 \cdot 10^{-12} T^{-2/3} \exp(-19.94 \cdot T^{-1/3}). \quad (1)$$

Since the previous correlation is appropriate for energy below or close to 25 keV, it should represent a reliable correlation to evaluate the reactivity for the plasma in ARC, featured by a peak temperature of 27 keV (see fig. 4).

The reaction rate distribution, expressed in reactions/(cm³s), can be evaluated thanks to the prior knowledge of the densities of deuterium and tritium and the reactivity distributions, using the following expression:

$$RR = n_D n_T (\overline{\sigma v})_{DT}. \quad (2)$$

Reminding that one neutron per reaction is produced, this result is equivalent to the neutron emission profile expressed in neutrons/(cm³s).

The resulting neutron emission profile, shown in fig. 5, is, as expected, many orders of magnitude lower in the plasma edge as compared to the values in the main plasma. Then, the

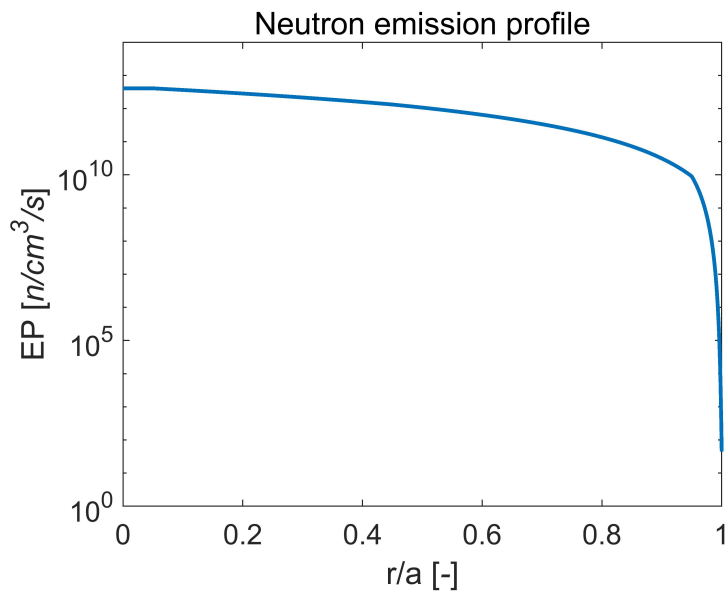


Fig. 5. Radial profile of neutron emission density in ARC.

plasma chamber has been divided in a series of concentric toroidal sub-domains, each one trying to simulate the toroidal magnetic surfaces of ARC, with the purpose of attributing the largest volume-average source weight to the innermost sub-domain and the lowest to the outermost one.

Once explained the rationale behind the calculations, it is now possible to exploit the neutron emission profile relation to estimate the volume-averaged neutron emission rate of the *i*-th toroidal

sub-domain with the following integral:

$$EP_{AVG_i} = \frac{1}{V_i} \int_{V_i} EP(r_i) d\mathbf{r}_i, \quad (3)$$

where $d\mathbf{r}_i$, for an axisymmetric torus, can be defined as:

$$d\mathbf{r}_i = 2\pi R_i r_i dr_i d\theta \quad (4)$$

$$R_i = R_0 + r_i \cos \theta. \quad (5)$$

R_0 is the major radius, θ is the polar angle coordinate and r_i is the minor radius coordinate. Defining $r_{in,i}$ and $r_{out,i}$ as the inner and outer radii of the i -th toroidal sub-domain, respectively, the final integral to be solved is:

$$EP_{AVG_i} = \frac{1}{V_i} \int_0^{2\pi} d\theta \int_{r_{in,i}}^{r_{out,i}} dr_i EP(r_i) 2\pi (R_0 + r_i \cos \theta) r_i, \quad (6)$$

where the term with $\cos \theta$ vanishes when integrating over θ . After all the simplifications, we obtain:

$$EP_{AVG_i} = \frac{4\pi^2 R_0}{V_i} \int_{r_{in,i}}^{r_{out,i}} EP(r_i) r_i dr_i. \quad (7)$$

The previous integral must be solved for each sub-domain in order to have the volume-averaged neutron emission rate in each sub-domain.

The number of sub-domains is a trade-off to balance the accuracy of the result and the complexity and the computational cost of the evaluation, due to an increasing number of sub-domains. The final choice is to consider 9 sub-domains starting from the centre of the plasma, defined as shown in table IV, with the corresponding volume-averaged emission rates.

II.C. Detectors definition and main settings for the simulations

Serpent is a Monte Carlo code, thus it allows to evaluate quantities of interest in terms of reaction rates or reaction rate densities thanks to the definition of detectors inside the domain, specifying a response function that represents the response of the detector and that can be modified choosing different reactions, either microscopic or macroscopic. Each type of reaction is identified by the so-called reaction MT number. In the case of microscopic reactions, all the MT nuclear

TABLE IV
Definition of the toroidal sub-domains for the source distribution.

	Radial position of the subdomain [cm]	EP_{AVG} [n/(cm ³ s)]
1 st subdomain	0 - 36	2.7294×10^{12}
2 nd subdomain	36 - 44	1.7645×10^{12}
3 rd subdomain	44 - 52	1.3805×10^{12}
4 th subdomain	52 - 60	1.0209×10^{12}
5 th subdomain	60 - 68	0.7121×10^{12}
6 th subdomain	68 - 76	0.4634×10^{12}
7 th subdomain	76 - 84	0.2725×10^{12}
8 th subdomain	84 - 92	0.1369×10^{12}
9 th subdomain	92 - 100	0.0524×10^{12}

reactions available in the ACE (A Compact ENDF) nuclear data files read by Serpent could be chosen.

The tritium production reactions have been evaluated using reaction number 205, while neutron and photon energy deposition with reaction number 80.

The total energy deposition tally allows to estimate the power deposited by neutrons, which depends on the reaction-wise KERMA (Kinetic Energy Release in Materials) coefficients available in the ACE data. Since the radiative captures involve the emission of photons, a coupled neutron-photon transport simulation is run in order to properly take into account the gamma rays spatial distribution inside the system. It is important to remark here that the version of Serpent employed for the calculations presented throughout the paper considers only photo-atomic interactions, neglecting photo-nuclear reactions.¹⁶ In any case, photo-nuclear reactions have high thresholds and are likely not relevant for the responses we have evaluated.

Serpent is equipped with detector types featured by shapes that are well suited for complex but very regular geometries, as the fuel assemblies of fission reactors. This is another important limitation, which complicates the definition of the detectors in a smart arrangement in order to obtain significant results concerning the distributions of the quantities of interest. Finally, a choice has been made to define a series of cylindrical detectors at different vertical locations, see fig. 6: approximately at the mid-plane, at the base of the upper divertor leg and above the upper divertor. Each detector has only one spatial bin in the vertical direction and one in the toroidal direction, since ARC can be considered axially symmetric. The only subdivision has been made in the radial direction, where it is expected that the quantities of interest have the most significant variations.

The vertical and radial dimensions of the bins have been chosen so that they are not too small, to avoid detrimental effects on the statistical error, and not too large, to achieve a good spatial resolution.

Due to the toroidal geometry of ARC, it is clear that each radial bin has the chance to vertically intersect different materials, thus the result associated with the bins are not only spatial averages, but also averages made on different materials. A possible solution to this shortcoming should be to reduce the vertical length of the detectors. However, this solution has not been pursued in the present work in order to avoid too high statistical errors with a reasonable computing time.

The detectors to evaluate the neutron flux distribution have been arranged in the domain as follows:

- a detector in the equatorial region with a vertical dimension of 20 cm and with its base coincident with the mid-plane of the reactor;
- a detector with the center at the height of 195 cm and a vertical dimension of 10 cm, at the base of the upper divertor leg;
- a detector in the polar region, above the upper divertor, between the vertical coordinates 341 cm and 360 cm, in order to include vertically the FLiBe blanket only.

Figure 6 schematizes the arrangement of the detectors in ARC. The same rationale has been used to define the detectors for the tritium production rate and for the power deposition estimation.

For the estimation of the power deposition, additional and smaller detectors have been located in the proximity of the vacuum vessel layers in order to obtain more refined radial distributions. In fact, this is the most important region for what concerns the power deposition, since it is the closest to the neutron source, where the deposited power is the maximum, with possible consequences on the structural integrity of the Inconel 718 vacuum vessel and on the cooling capability of the FLiBe cooling channel.

Concerning the TBR, in principle it is sufficient to define a detector coincident with the whole domain, since the breeding of tritium is a global quantity. However, a series of different detectors, similar to the ones defined for the neutron flux, has been set, in order to distinguish the contribution of the two lithium isotopes, ${}^6\text{Li}$ and ${}^7\text{Li}$, in the reactor.

In addition to these detectors, useful for the evaluation of radial distributions, other cell

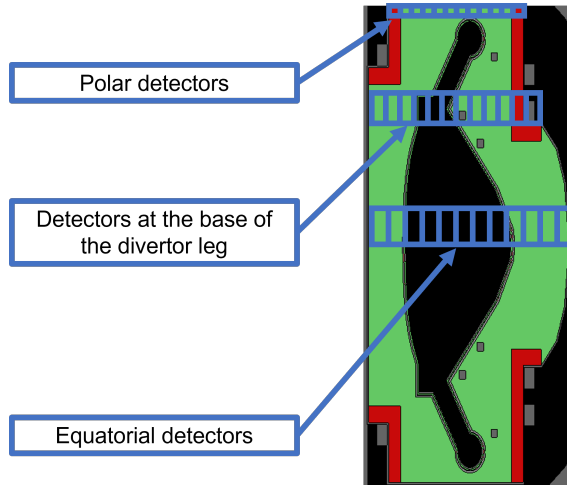


Fig. 6. Qualitative sketch of the series of cylindrical ($r\theta z$) detectors defined in the reactor domain in order to evaluate the quantities of interest at different radial and vertical positions. The toroidal coordinate is not considered because of the axial-symmetry of ARC. The dimensions of the detectors are not to scale.

detectors for the estimation of average quantities have been defined. For example, each layer of the vacuum vessel has been associated with a detector in order to obtain an estimation of the average volumetric power deposited by neutrons and photons on each layer. These results are useful to perform comparison with literature results and to get a more immediate, even if less refined, information.

In order to obtain results from the previously defined detectors, the total number of neutron histories simulated in the neutron-photon coupled transport simulation is 10^8 , divided into 100 batches. This is a reasonable choice with the available computing power and considering that a further increase of the number of histories would increase too much the computational power, with minor benefits in terms of statistical error.

The nuclear data library used for the transport simulation is the ENDF/B-VIII.0 library, the most updated among the ENDF libraries currently available.¹⁷

III. RESULTS

This section presents the results obtained with the Serpent simulations in terms of neutron flux, TBR, and volumetric power deposition, for both cases with a spatially uniform source and a non-uniform one. The TBR (subsection III.B) and the power deposition (subsection III.C) are

presented for the case with the non-uniform source, as it can be considered more realistic, while the neutron flux results (subsection III.A) are shown for both cases to evidence the differences as they appear more visible.

The scripts employed to obtain the results presented in the following subsections are available in a Zenodo repository.¹⁸

III.A. Neutron flux

The first quantity evaluated is the neutron flux, since it is the quantity all the reaction rates depend on. The neutron flux is evaluated at different vertical locations, as previously explained. The results, with the subdivision between the different components of ARC represented by dashed lines, are summarized in fig. 7. The radial profile of the neutron flux at the mid-plane of ARC for the non-uniform source (fig. 7(a)) is consistent with the definition of the source. The main difference at the base of the upper divertor leg (fig. 7(c)) is that, in this region, the neutron flux obtained with the non-uniform source is smaller because it is located farther from the centre of the plasma and there is a smaller number of neutrons, consistently with the source definition. Finally, the profiles of the neutron flux in the blanket above the upper divertor (fig. 7(e)) are similar in shape but different in amplitude, for the same reason as stated above. The localized peak is due to the neutron streaming from the divertor region.

The error bars are not visible on a linear scale, because only the bins where the relative error is smaller than 5% have been kept, even if they are actually present and would be relatively non-negligible in the peripheral regions of ARC. The same kind of features and considerations can be made for the results relative to the tritium production rate TBR (subsection. III.B) and the power deposition (subsection. III.C), as these quantities depend on the neutron flux. For further analysis of the neutron flux far from the breeding blanket, e.g. for activation purposes, variance reduction methods could be extremely helpful in reducing the statistical errors.

Fig. 8(a) shows the neutron flux as a function of energy, evaluated with a cell detector in each component over 500 energy bins equally-spaced in lethargy, which is a quantity of paramount importance in order to provide a physical insight of the neutronic energy behaviour in the reactor. The neutron flux in the outer blanket tank surface is orders of magnitude lower than in the breeding blanket, underlining again the shielding effect of the FLiBe blanket. Moreover, the flux in the

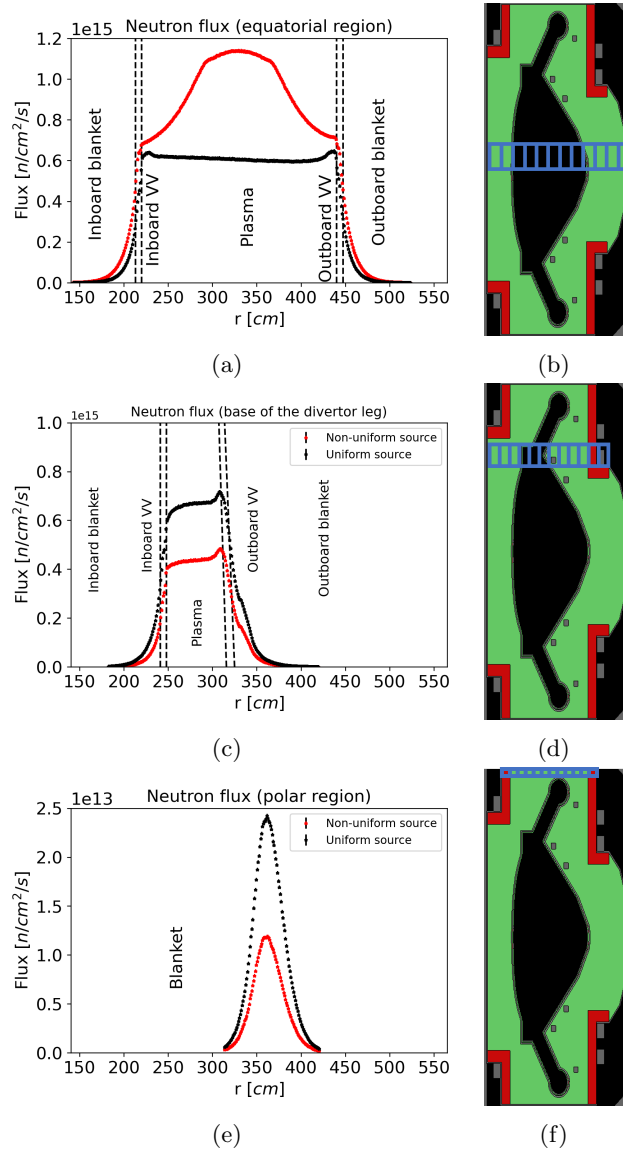


Fig. 7. Neutron flux in the equatorial region (a), at the base of the upper divertor leg (c) and above the upper divertor (e), on a linear scale, and respective positions of the detectors (right column). The error bars are too small and thus not visible (the maximum relative error is in the order of 5%).

neutron multiplier is the highest, consistently with the role played by this component in increasing the number of neutrons. Another observable feature is the peak in correspondence to 14.1 MeV, which is the fusion source emission energy. The peculiar shape of the flux in the blanket, featured by a series of spikes in correspondence of the main resonance peaks of the nuclides composing the salt (fig. 8(b)), is comparable to the one observed in Molten Salt Fast Reactors (MSFR) using

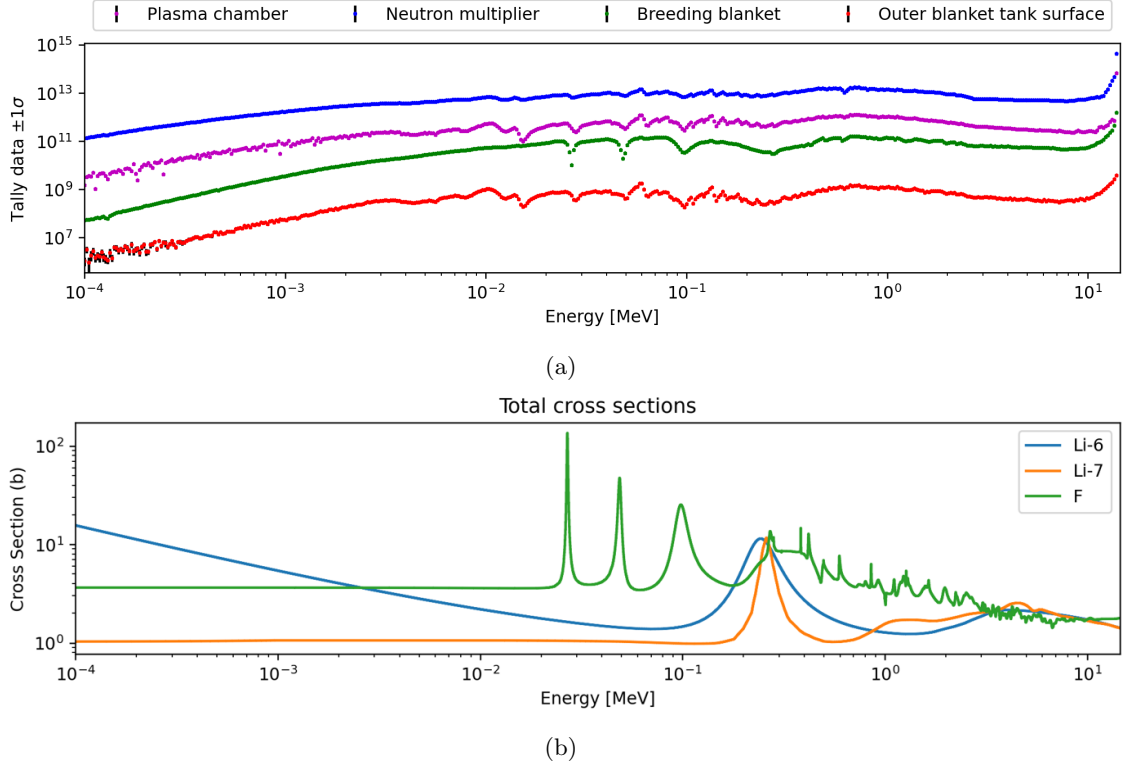


Fig. 8. (a): neutron flux as a function of energy in the plasma chamber, neutron multiplier, breeding blanket and outer blanket tank surface (a). The error bars are visible only for the outer blanket tank surface, as for the other components the statistical error is too low (except for the blanket tank, the maximum relative error is 6.124%, found in the plasma chamber, see¹⁸). (b): total microscopic cross sections as a function of energy for the fluorine, ^6Li and ^7Li isotopes, evaluated using the ENDFB/VIII library and at their respective enrichment in ARC's FLiBe.

similar salts.¹⁹

III.B. Tritium breeding ratio

The TBR is, by definition, a global parameter, thus it can be evaluated using a single detector covering the whole machine. The results obtained with Serpent for the two sources are shown in table V and are comparable with the result obtained in a previous study.¹¹

In table V it is possible to observe that the contribution of the cooling channel to the TBR is substantial, in spite it amounts to around 1% of the total blanket volume, suggesting that an improvement in the design of the cooling channel itself might further increase the TBR.¹² On the contrary, it seems that the amount of tritium produced in the blanket is mainly due to its large volume, as the neutron flux decays exponentially in the blanket.

TABLE V

Global values of TBR for the uniform and non-uniform sources in the cooling channel and breeding blanket of ARC, compared with literature values¹.

	Cooling Channel	Breeding blanket	Total
Uniform source	0.2717(1)	0.8104(1)	1.0845(1)
Non-uniform source	0.2526(1)	0.8303(1)	1.0853(2)
Reference ¹¹			1.080(4)

¹ The number in parenthesis has to be applied as a \pm on the last digit of the result.

Another interesting result is the partial contribution of ${}^6\text{Li}$ versus ${}^7\text{Li}$ to the radial reaction rate, as shown in fig. 9. The contribution of ${}^6\text{Li}$ is some orders of magnitude higher, as the

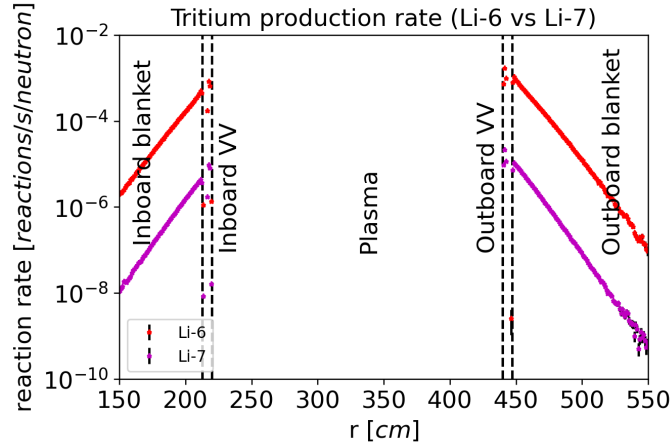


Fig. 9. Radial distribution of the reaction rate relative to ${}^7\text{Li}$ and to ${}^6\text{Li}$ in the equatorial region for the non-uniform source on a logarithmic scale.

FLiBe salt in ARC is isotopically enriched with 90% of ${}^6\text{Li}$ and its cross section is higher also for lower neutron energies, while ${}^7\text{Li}$ presents a threshold behavior and only neutrons with energies higher than 2.466 MeV have the chance to react with ${}^7\text{Li}$ and produce tritium. However, the presence of ${}^7\text{Li}$ is anyway important because a secondary result of its interaction with a neutron is the generation of another neutron, partly compensating for the neutrons losses by absorption in structural materials and leakages.

III.C. Power deposition

Initially, the average volumetric power deposition in the main components of ARC has been evaluated with Serpent (table VI) and compared with literature results.¹¹ The average power

TABLE VI

Average volumetric power deposition and total power deposition in each material layer in the ARC reactor with the uniform source (U) and the non-uniform source (NU).¹

	Vol. power (U) [MW/m ³]	Vol. power (NU) [MW/m ³]	Vol. power ¹¹ [MW/m ³]	Power (U) [MW]	Power (NU) [MW]	Power ¹¹ [MW]
FW ²	26.526(8)	23.165(7)	24.1	8.488(3)	7.413(2)	8.4
IVV ²	12.736(2)	10.908(2)	11.3	41.646(7)	35.669(6)	39.6
CC ²	13.043(2)	12.020(2)	11.0	85.82(1)	79.09(1)	77.7
NM ²	6.772(1)	6.526(1)	6.3	22.415(4)	21.602(4)	22.4
OVV ²	7.418(1)	7.318(1)	7.4	74.33(1)	73.33(1)	78.8
FB ²	0.7815(1)	0.8388(8)	1.1	237.58(3)	255.02(3)	255.0
PFCS ²	0.0035(1)	0.00277(1)	0.04	0.1523(6)	0.1205(5)	1.8
Total				475.78(3)	476.04(3)	484

¹ The number in parenthesis has to be applied as a \pm on the last digit of the result.

² FW = first wall, IVV = inner vacuum vessel, CC = cooling channel, NM = neutron multiplier, OVV = outer vacuum vessel, FB = FLiBe blanket, PFCS = poloidal field coil shielding.

deposition, expressed in MW, has been obtained simply multiplying the average volumetric power deposition by the volume of each component (table II).

Observing the power deposition, the relative difference with the results found in the literature are below the 10%, except for the PF coil shielding. This is a particular component since it is located far from the neutron source and, for this reason, the statistics is quite poor. However, no particular effort has been made to improve the statistics related to the power deposited on the PF coil shielding as it does not contribute significantly to the power generation of ARC.

Another aspect to be observed is that the total power deposition estimated with Serpent, around 475 MW, is larger than the power of the neutrons emitted by the fusion reactions of ARC (425 MW). This is reasonable primarily because of exothermic reactions between neutrons and ⁶Li (Ref. 11) and the presence of beryllium as neutron multiplier.

As explained in subsection II.C, the simulations performed in this work consider both neutrons and photons. Thus, it is possible to separate their contribution to the power deposition and the results are presented in table VII. In general, photons deposit a larger amount of power in heavier materials (like the tungsten of the first wall and the Inconel 718 of the vacuum vessel) but,

TABLE VII

Contribution of neutrons and photons to the average volumetric power deposition for the uniform (U) and non-uniform (NU) source.¹

	Neutrons (U) [MW/m ³]	Photons (U) [MW/m ³]	Neutrons (NU) [MW/m ³]	Photons (NU) [MW/m ³]
FW ²	1.1616(4)	25.364(8)	0.9000(3)	22.265(7)
IVV ²	5.4268(8)	7.309(2)	4.4587(7)	6.449(1)
CC ²	11.683(2)	1.3601(4)	10.786(2)	1.2341(4)
NM ²	5.716(1)	1.0559(4)	5.548(1)	0.9782(4)
OVV ²	2.2547(3)	5.1633(9)	2.3362(3)	4.9817(9)
FB ²	0.6623(1)	0.1192(1)	0.71398(8)	0.12486(2)
PFCS ²	0.000566(4)	0.00293(1)	0.000405(3)	0.00236(1)

¹ The number in parenthesis has to be applied as a \pm on the last digit of the result.

² FW = first wall, IVV = inner vacuum vessel, CC = cooling channel, NM = neutron multiplier, OVV = outer vacuum vessel, FB = FLiBe blanket, PFCS = poloidal field coil shielding

since the volumetric power deposition of neutrons in the blanket, which is the largest component, is higher, the total contribution of neutrons is predominant (table VIII). The results proves that

TABLE VIII

Contribution of neutrons and photons to the total power deposition inside the blanket tank for the uniform and the non-uniform sources¹.

	Neutrons [MW]	Photons [MW]	Total [MW]
Uniform source	338.75(2)	137.03(2)	476.04(3)
Non-uniform source	345.30(3)	130.74(2)	475.78(3)

¹ The number in parenthesis has to be applied as a \pm on the last digit of the result.

the photon contribution to the overall power deposition is important and, therefore, should not be neglected.

Aside from average estimations of the power deposition in the components, it is necessary to know its radial distribution in different regions of the reactor too, in order to verify that structural integrity is preserved in all the points. The profile at the mid-plane (fig. 10) presents two peaks in correspondence of the first medium encountered by the neutrons, i.e. the vacuum vessel, and then it decays in an exponential way in the blanket, as expected. It is of major interest to evaluate in detail the deposited power in the layers of the vacuum vessel (fig. 11), where the values are the highest and there are different materials. The highest values are in correspondence of the first

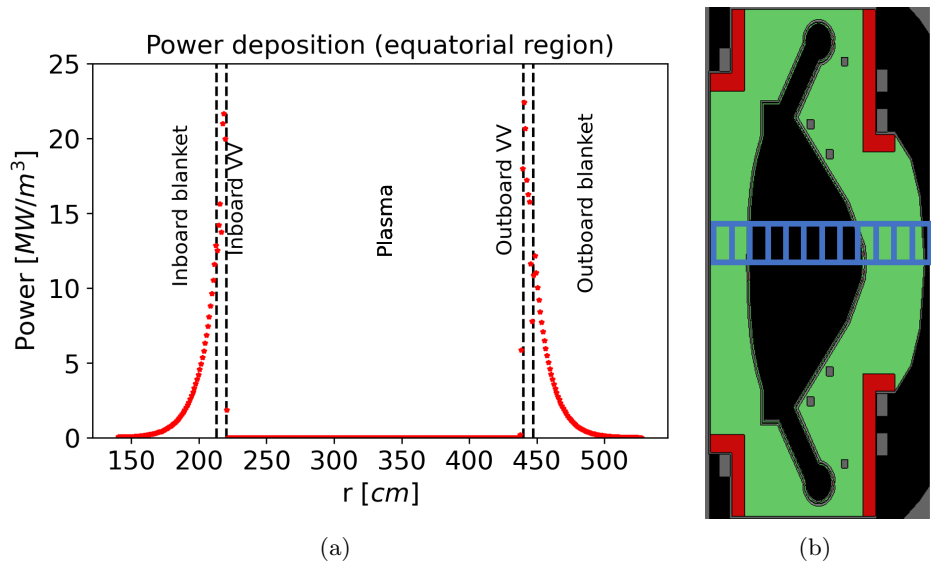


Fig. 10. Radial volumetric power deposition in the equatorial region (a) and position of the detector (b) for the non-uniform source. The error bars are not visible because the scale is linear and the maximum relative error is in the order of 5%.

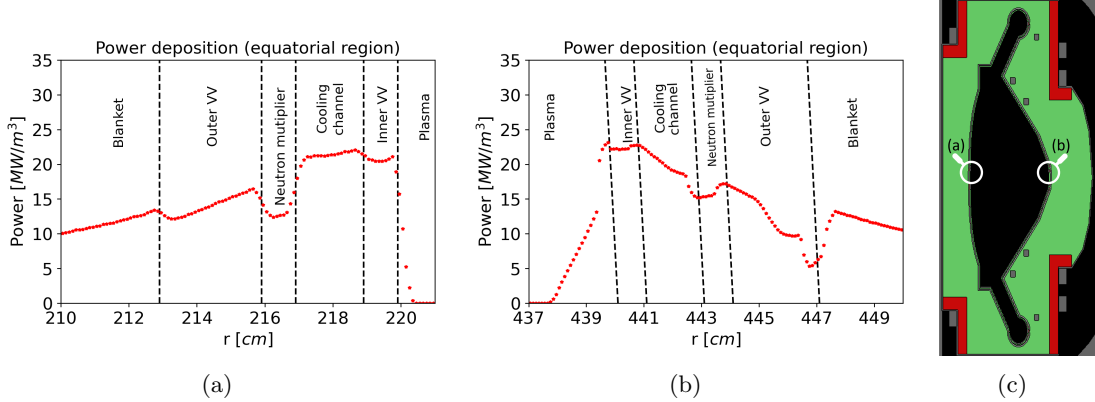


Fig. 11. Radial power deposition in the equatorial region on the inboard (a) and outboard (b) side of the vacuum vessel and positions of the detectors (c) for the non-uniform source. The error bars are not visible because the relative error is too low (the maximum relative error is 2.085%, see the Zenodo repository¹⁸).

wall and the first layer of the vacuum vessel, then the volumetric power deposition progressively decays. Similar considerations can be made at a different vertical position, at the base of the upper divertor leg, see fig. 12. In absolute terms, the power deposition in this region is smaller, simply because the source of neutrons considered in this case is the non-uniform one, which is peaked at the centre of the plasma.

Considering the detail of the layer of the vacuum vessel (fig. 13), the main difference is that

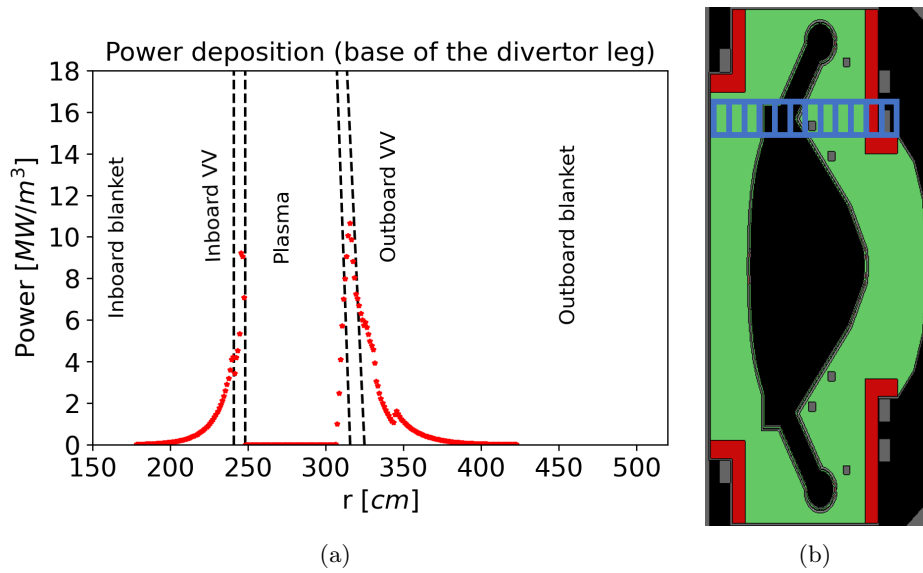


Fig. 12. Radial volumetric power deposition at the base of the upper divertor leg (a) and position of the detector (b) for the non-uniform source. The error bars are not visible because the scale is linear and the maximum relative error is in the order of 5%.

on the outboard side of the vacuum vessel no drop passing from a medium to another is observed. This is because this side of the vessel has a curvature such that the vertical dimension of the detectors intersects different materials at a given radial coordinate. Thus, the results displayed in the plot represent an average value performed on different materials, as mentioned above.

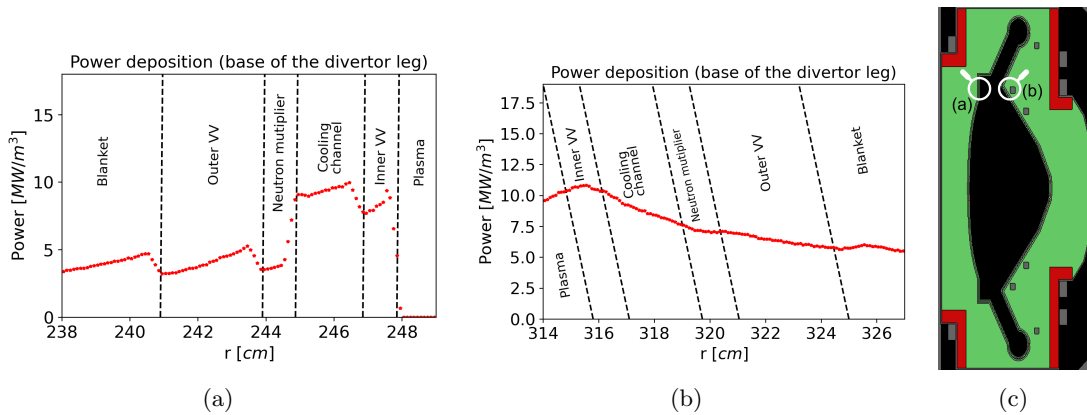


Fig. 13. Radial power deposition at the base of the upper divertor leg on the inboard (a) and outboard (b) side of the vacuum vessel and positions of the detectors (c) for the non-uniform source. The error bars are not visible because the relative error is too low (the maximum relative error is 2.291%, see the Zenodo repository¹⁸).

Finally, the power deposition in the blanket above the upper divertor leg (fig. 14) has a peak

in correspondence of the divertor and lower values, as expected.

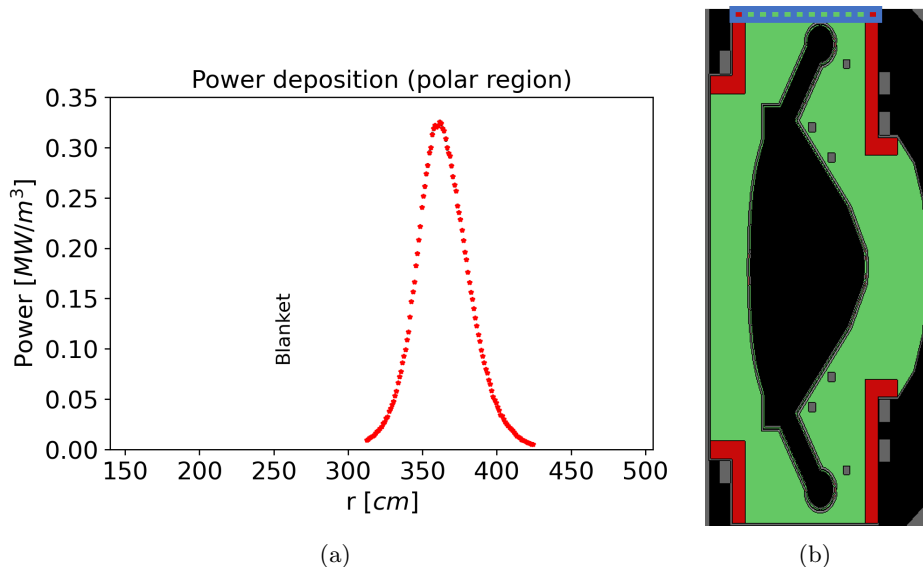


Fig. 14. Radial volumetric power deposition above the upper divertor (a) and position of the detector (b) for the non-uniform source. The error bars are not visible because the scale is linear and the maximum relative error is in the order of 5%.

IV. CONCLUSIONS

In this work, the Monte Carlo particle transport code Serpent has been employed for the neutronic analysis of the fusion reactor ARC, with the aim of evaluating the TBR global parameter and the power deposition distribution in the breeding blanket.

Serpent has been used mainly for the analysis of fission systems in the past. For this reason, one of the main goals of this work was to understand if the use of Serpent for fusion reactors modelling yields acceptable results with respect to the available literature.

A first set of simulations has been performed using a spatially uniform source inside the plasma chamber. Afterwards, a second set of calculations with a spatially non-uniform and more realistic source, obtained defining a series of concentric toroidal sub-domains with different weights, has been carried out. Neither of the two definitions could fully catch the actual plasma physics details of ARC, which is a much more complex aspect not taken into account in this work.

The results obtained for what concerns the TBR and the power deposition are consistent with the physics of the problem and comparable with the results in the fusion community literature,

where the most adopted code is MCNP. The relative differences between the total power deposition values estimated in this work are in the order of 10% with respect to the literature ones, for the components of interest. The TBR obtained with Serpent differs from the literature value by a relative difference of 0.49% and is equal to 1.08, which may be sufficient depending on the tritium extraction system efficiency and required doubling time.

However, the value of the calculated TBR obtained in the present work does not take into account the tritium losses, the inefficiencies of the tritium extraction systems and the uncertainties related to the nuclear data. Thus, it is possible that the achievable TBR will not actually be larger than one.

In future works, a multi-physics model coupling the Serpent neutronic model with a CFD/MHD model will be necessary for a thorough thermal-hydraulic analysis of the FLiBe flow and pressure fields, and for taking into account the effect of the temperature field on the cross sections.

In the spirit of the Best Estimate Plus Uncertainty approach, the results should be complemented with an uncertainty quantification (UQ) analysis. This is particularly important in this context because of the presence of lithium and fluorine, whose nuclear data could be affected by considerable uncertainty, due to their unconventional use in traditional nuclear systems, and of the high energy range of fusion neutrons, potentially resulting in an achievable TBR smaller than one. As Serpent does not allow to perform the UQ in the case of the external source mode, alternative non-intrusive approaches will need to be adopted (e.g. Polynomial Chaos Expansion).

REFERENCES

- [1] B. SORBOM, J. BALL, T. PALMER, F. MANGIAROTTI, J. SIERCHIO, P. BONOLI, C. KASTEN, D. SUTHERLAND, H. BARNARD, C. HAAKONSEN, J. GOH, C. SUNG, and D. WHYTE, “ARC: A compact, high-field, fusion nuclear science facility and demonstration power plant with demountable magnets,” *Fusion Engineering and Design*, **100**, 378 (2015).
- [2] A. J. H. DONNÉ, W. MORRIS, X. LITAUDON, C. HIDALGO, D. McDONALD, H. ZOHRM, E. DIEGELE, A. MÖSLANG, K. H. NORDLUND, G. FEDERICI, P. SONATO, C. WALDON, D. BORBA, and P. HELANDER, *European Research Roadmap to the Realisation of Fusion Energy*, EUROfusion Consortium, Germany (2018).
- [3] J. LEPPÄNEN, M. PUSA, V. T. V. VALTAVIRTA, and T. KALTIAISENAHO, “The Serpent

- Monte Carlo code: Status, development and applications in 2013,” *Annals of Nuclear Energy*, **82**, 142 (2013).
- [4] J. GORLEY, “Initial MCNP6 Release Overview - MCNP6 version 1.0.” LA-UR-13-22934 (2013).
- [5] Y. LU, G. ZHOU, F. A. HERNÁNDEZ, P. PERESLAVTSEV, J. LEPPÄNEN, and M. YE, “Benchmark of Serpent-2 with MCNP: application to European DEMO HCPB breeding blanket,” *Fusion Engineering and Design*, **155** (2020).
- [6] A. VALENTINE, B. COLLING, R. WORRALL, and J. LEPPÄNEN, “Benchmarking of the Serpent 2 Monte Carlo Code for Fusion Neutronics Applications,” *EPJ Web of Conferences*, **247**, 04015 (2021); 10.1051/epjconf/202124704015.
- [7] A. TURNER, A. BURNS, B. COLLING, and J. LEPPÄNEN, “Applications of Serpent 2 Monte Carlo Code to ITER Neutronics Analysis,” *Fusion Science and Technology*, **74**, 4, 315 (2018); 10.1080/15361055.2018.1489660., URL <https://doi.org/10.1080/15361055.2018.1489660>.
- [8] NALLO, G. F., ABRATE, N., DULLA, S., RAVETTO, P., and VALERIO, D., “Neutronic benchmark of the FRENETIC code for the multiphysics analysis of lead fast reactors,” *The European Physical Journal Plus*, **135** (2020).
- [9] ABRATE, N., AUFIERO, M., DULLA, S., and FIORITO, L., “Nuclear data uncertainty quantification in molten salt reactors with XGPT,” *International Conference on Mathematics Computational Methods and Reactor Physics* (2019).
- [10] “SolidWorks User’s Manual,” URL <https://www.solidworks.com>.
- [11] A. KUANG, N. CAO, A. CREELY, C. DENNETT, J. HECLA, B. LABOMBARD, R. TINGUELY, E. TOLMAN, H. HOFFMAN, M. MAJOR, J. R. RUIZ, D. BRUNNER, P. GROVER, C. LAUGHMAN, B. SORBOM, and D. WHYTE, “Conceptual design study for heat exhaust management in the ARC fusion pilot plant,” *Fusion Engineering and Design*, **137**, 221 (2018).
- [12] S. SEGANTIN, R. TESTONI, Z. HARTWIG, D. WHYTE, and M. ZUCCHETTI, “Optimization of tritium breeding ratio in ARC reactor,” *Fusion Engineering and Design*, **154**, 111531 (2020).

- [13] R. TUOMINEN, V. VALTAVIRTA, J. PELTOLA, and J. LEPPÄNEN, “Coupling Serpent and OpenFOAM for neutronics - CFD multi-physics calculations,” *PHYSOR 2016: Unifying Theory and Experiments in the 21st Century*, 255–269, American Nuclear Society (ANS), United States (2016)SDA: SHP: SASUNE Nuclear Project : 100502 ; International Conference on the Physics of Reactors, PHYSOR 2016 : Unifying Theory and Experiments in the 21st Century, PHYSOR 2016 ; Conference date: 01-05-2016 Through 05-05-2016.
- [14] J.-C. JABOULAY, F. DAMIAN, G. AIELLO, D. TAYLOR, S. ZHENG, B. BIENKOWSKA, K. DROZDOWICZ, G. TRACZ, U. FISCHER, and C. BACHMANN, “Monte Carlo tools evaluation for nuclear analyses of the European DEMO,” *Fusion Engineering and Design*, **98-99**, 1800 (2015)Proceedings of the 28th Symposium On Fusion Technology (SOFT-28).
- [15] J. HUBA, NRL *plasma formulary*, The Office of Naval Research (2002).
- [16] R. TUOMINEN, V. VALTAVIRTA, and J. LEPPÄNEN, “New energy deposition treatment in the Serpent 2 Monte Carlo transport code,” *Annals of Nuclear Energy*, **129**, 224 (2019).
- [17] D. A. BROWN, M. B. CHADWICK, R. CAPOTE, A. C. KAHLER, A. TRKOV, M. W. HERMAN, A. A. SONZOGNI, Y. DANON, A. D. CARLSON, M. DUNN, D. L. SMITH, G. M. HALE, G. ARBANAS, R. ARCILLA, C. R. BATES, B. BECK, B. BECKER, F. BROWN, R. J. CASPERSON, J. CONLIN, D. E. CULLEN, M. A. DESCALLE, R. FIRESTONE, T. GAINES, K. H. GUBER, A. I. HAWARI, J. HOLMES, T. D. JOHNSON, T. KAWANO, B. C. KIEDROWSKI, A. J. KONING, S. KOPECKY, L. LEAL, J. P. LESTONE, C. LUBITZ, J. I. MÁRQUEZ DAMIÁN, C. M. MATTOON, E. A. MCCUTCHAN, S. MUGHABGHAB, P. NAVRATIL, D. NEUDECKER, G. P. A. NOBRE, G. NOGUERE, M. PARIS, M. T. PIGNI, A. J. PLOMPEN, B. PRITYCHENKO, V. G. PRONYAEV, D. ROUBTSOV, D. ROCHMAN, P. ROMANO, P. SCHILLEBEECKX, S. SIMAKOV, M. SIN, I. SIRAKOV, B. SLEAFORD, V. SOBES, E. S. SOUKHOVITSKII, I. STETCU, P. TALOU, I. THOMPSON, S. VAN DER MARCK, L. WELSER-SHERRILL, D. WIARDA, M. WHITE, J. L. WORMALD, R. Q. WRIGHT, M. ZERKLE, G. ŽEROVNIK, and Y. ZHU, “ENDF/B-VIII.0: The 8th Major Release of the Nuclear Reaction Data Library with CIELO-project Cross Sections, New Standards and Thermal Scattering Data,” *Nuclear Data Sheets*, **148**, 1 (2018).
- [18] A. AIMETTA, “Neutronic analysis of the fusion reactor ARC: Monte Carlo simulations with the

Serpent code,” (2020); 10.5281/zenodo.5118690., URL <https://doi.org/10.5281/zenodo.5118690>.

[19] BROVCHENKO, M., KLOOSTERMAN, J. L., LUZZI, L., MERLE, E., HEUER, D., LAUREAU, A., FEYNBERG, O., IGNATIEV, V., AUFIERO, M., CAMMI, A., FIORINA, C., ALCARO, F., DULLA, S., RAVETTO, P., FRIMA, L., LATHOUWERS, D., and MERK, B., “Neutronic benchmark of the molten salt fast reactor in the frame of the EVOL and MARS collaborative projects,” *EPJ Nuclear Science & Technology*, **5** (2019).

LIST OF FIGURES

1	ARC assembling scheme (reproduced from ¹).	3
2	Poloidal section of ARC generated with the CAD model and implemented in Serpent (a), and detail of the radial build of the double wall vacuum vessel (b). From the right to the left: plasma chamber (black), first wall (blue), inner vacuum vessel (grey), cooling channel (green), neutron multiplier (red), outer vacuum vessel (grey) and FLiBe blanket (green).	7
3	Temperature distribution across the vacuum vessel (with the plasma-facing surface on right) at both the channel inlet and outlet, evaluated with a COMSOL model (reproduced from ¹).	8
4	Radial profiles of electron temperature and electron density in ARC (reproduced from ¹)	9
5	Radial profile of neutron emission density in ARC.	10
6	Qualitative sketch of the series of cylindrical ($r\theta z$) detectors defined in the reactor domain in order to evaluate the quantities of interest at different radial and vertical positions. The toroidal coordinate is not considered because of the axial-symmetry of ARC. The dimensions of the detectors are not to scale.	14
7	Neutron flux in the equatorial region (a), at the base of the upper divertor leg (c) and above the upper divertor (e), on a linear scale, and respective positions of the detectors (right column). The error bars are too small and thus not visible (the maximum relative error is in the order of 5%).	16

8	(a): neutron flux as a function of energy in the plasma chamber, neutron multiplier, breeding blanket and outer blanket tank surface (a). The error bars are visible only for the outer blanket tank surface, as for the other components the statistical error is too low (except for the blanket tank, the maximum relative error is 6.124%, found in the plasma chamber, see ¹⁸). (b): total microscopic cross sections as a function of energy for the fluorine, ⁶ Li and ⁷ Li isotopes, evaluated using the ENDFB/VIII library and at their respective enrichment in ARC's FLiBe.	17
9	Radial distribution of the reaction rate relative to ⁷ Li and to ⁶ Li in the equatorial region for the non-uniform source on a logarithmic scale.	18
10	Radial volumetric power deposition in the equatorial region (a) and position of the detector (b) for the non-uniform source. The error bars are not visible because the scale is linear and the maximum relative error is in the order of 5%.	21
11	Radial power deposition in the equatorial region on the inboard (a) and outboard (b) side of the vacuum vessel and positions of the detectors (c) for the non-uniform source. The error bars are not visible because the relative error is too low (the maximum relative error is 2.085%, see the Zenodo repository ¹⁸).	21
12	Radial volumetric power deposition at the base of the upper divertor leg (a) and position of the detector (b) for the non-uniform source. The error bars are not visible because the scale is linear and the maximum relative error is in the order of 5%.	22
13	Radial power deposition at the base of the upper divertor leg on the inboard (a) and outboard (b) side of the vacuum vessel and positions of the detectors (c) for the non-uniform source. The error bars are not visible because the relative error is too low (the maximum relative error is 2.291%, see the Zenodo repository ¹⁸).	22
14	Radial volumetric power deposition above the upper divertor (a) and position of the detector (b) for the non-uniform source. The error bars are not visible because the scale is linear and the maximum relative error is in the order of 5%.	23

LIST OF TABLES

I	Radial thickness of the double vacuum vessel layers. ¹¹	5
---	--	---

II	Volumes of each material layer in the ARC reactor.	6
III	Main dimensions of the ARC reactor adopted in the CAD model.	6
IV	Definition of the toroidal sub-domains for the source distribution.	12
V	Global values of TBR for the uniform and non-uniform sources in the cooling channel and breeding blanket of ARC, compared with literature values.	18
VI	Average volumetric power deposition and total power deposition in each material layer in the ARC reactor with the uniform source (U) and the non-uniform source (NU).	19
VII	Contribution of neutrons and photons to the average volumetric power deposition for the uniform (U) and non-uniform (NU) source.	20
VIII	Contribution of neutrons and photons to the total power deposition inside the blanket tank for the uniform and the non-uniform sources.	20